Theoretical Investigation of Raman Optical Activity Signatures of Troger's Base

ARTICLE *in* THE JOURNAL OF PHYSICAL CHEMISTRY A · OCTOBER 2011

Impact Factor: 2.69 · DOI: 10.1021/jp208591j · Source: PubMed

2 AUTHORS:

Vincent Liégeois
University of Namur
37 PUBLICATIONS **453** CITATIONS
SEE PROFILE

Benoît Champagne
University of Namur
401 PUBLICATIONS **8,719** CITATIONS
SEE PROFILE

THE JOURNAL OF PHYSICAL CHEMISTRY A

ARTICLE

pubs.acs.org/JPCA

Theoretical Investigation of Raman Optical Activity Signatures of Tröger's Base

Vincent Liégeois* and Benoît Champagne

Laboratoire de Chimie Théorique, Facultés Universitaires Notre-Dame de la Paix, rue de Bruxelles, 61, B-5000 Namur, Belgium

ABSTRACT: The Raman and VROA spectra of (*S*,*S*)-Tröger's base are simulated. We mainly discuss the peaks in the 1140−1400 cm^{-1} wavenumber range where an intense VROA signature is found. In this range, nearly all of the Raman-active bands belong to the irreducible representation A (C_2 point group), whereas no such observation is made for the VROA spectrum. The vibrational normal modes associated with the peaks in this range mainly consist of wagging and twisting motions of the hydrogen atoms. From the atomic contribution patterns (ACPs) and the group coupling matrices (GCMs), one finds that the VROA backward-scattering intensities mainly arise from hydrogen and carbon atoms in the vicinity of the two chiral nitrogen atoms. The VROA signatures in the 1140−1400 cm^{-1} range are therefore a fingerprint of the local chirality around the two chiral nitrogen centers.

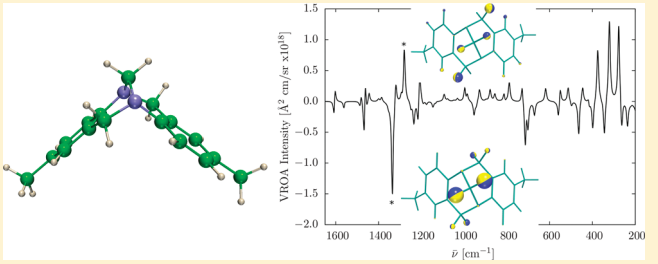

1. INTRODUCTION

Tröger's base[1] is an interesting chiral molecule because of its peculiar chirality origin and shape. Indeed, it is the first chiral tertiary amine free of non-nitrogen stereogenic centers to have been resolved.[2] Usually, tertiary amine molecules racemize quickly through inversion at the nitrogen atom, but this inversion is not possible in Tröger's base because of its rigidity. Moreover, its λ shape has recently gained interest because it can avoid $\pi-\pi$ close stacking, as well as a centrosymmetric arrangement, and it can thus match requirements for optoelectronics[3−5] or nonlinear optics materials.[6,7] Tröger's base derivatives are also used for chiral recognition.[8] A review by Sergeyev[9] summarizes the story of Tröger's base and its applications.

The determination of the absolute configuration of Tröger's base was not a trivial task, and it was even incorrectly predicted by Mason et al. in 1967[10] from near-ultraviolet electronic circular dichroism (CD). In fact, it was not until the X-ray structure had been determined that the correct assignment was obtained. At first, the X-ray structure of the racemic mixture was reported by Wilcox and Larson[11] and Wilcox.[12] In 1991, the X-ray structure of a salt containing monoprotonated (+)-Tröger's base with the monoanion of (−)-1,1′-binaphthalene-2,2′-diyl hydrogen phosphate unambiguously indicated that (+)-Tröger's base has the (*S*,*S*) absolute configuration.[13] Vibrational circular dichroism (VCD) measurements and calculations later confirmed this assignment.[14,15]

Vibrational Raman optical activity (VROA) spectroscopy[16−18] is complementary to vibrational circular dichroism (VCD) and is a powerful technique for studying both the configurations and conformations of molecules and macromolecules. One of the subjects of study for VROA spectroscopy is biomolecules.[19−31] More recently, simulated VROA spectra have appeared for chiral transition metal complexes,[32,33] followed by experimental measurements.[34] Other studies have focused on small molecules[35−37] or on synthetic polymers[38−40] looking for helicity signatures. Currently, one of the main challenges for VROA spectroscopy is to provide a catalogue of general rules that can be used to interpret dominant spectral signatures, just as has been accomplished for IR and Raman spectroscopies.

Herein, we present an analysis of the VROA signatures of Tröger's base using ab initio methods. Moreover, various tools such as the atomic contribution patterns, group coupling matrices, and similarities between vibrational normal modes are used to unravel the origin of the VROA signatures for this typical C_2 molecule.

2. VROA THEORY

Vibrational Raman optical activity (VROA) spectroscopy measures the tiny difference in Raman scattering between right- and left-handed incident circularly polarized light (ICP scheme). In the measurement, the time-average power of the photons scattered within a cone of solid angle $d\Omega$, called the radiant intensity I (J s^{-1} sr^{-1}), is recorded. This intensity is proportional to the time-average energy flux of the incident beam, called the irradiance $\mathcal{I}$ (J s^{-1} m^{-2}): $I = (d\sigma/d\Omega)\mathcal{I}$, where the factor of proportionality is called the differential scattering cross section (m^2/sr) and is the quantity calculated by ab initio methods. Within the harmonic approximation, the differential VROA scattering cross section for a naturally

Received: September 6, 2011
Revised: October 3, 2011
Published: October 03, 2011

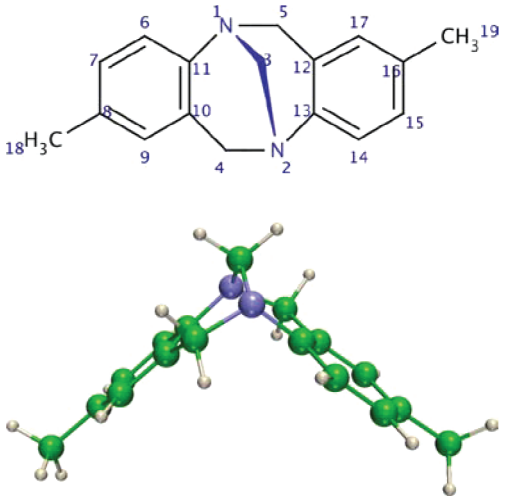

Figure 1. (Top) Two-dimensional sketch and (bottom) B3LYP/6-31G*-optimized structure of (*S*,*S*)-Tröger's base.

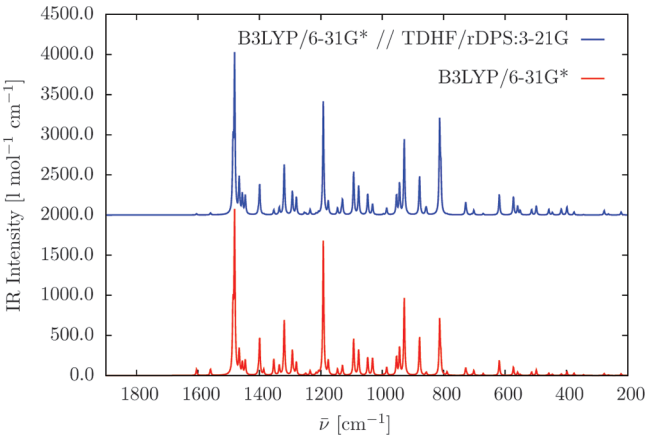

Figure 2. Simulated IR spectra of (*S*,*S*)-Tröger's base. The vibrational normal coordinates were evaluated at the B3LYP/6-31G* level, whereas the polarizabilities and their geometrical derivatives were evaluated at the (top) TDHF/rDPS:3-21G or (bottom) B3LYP/6-31G* level. Each transition is represented by a Lorentzian function with a fwhm of 4 cm^{-1}. A multiplicative factor of 0.96 was used to scale the vibrational frequencies.

polarized incident light (n) in the scattered circularly polarized (SCP) scheme for a scattering angle θ and the pth vibrational normal mode reads[16−18]

$$-\Delta^{n}\, d\sigma(\theta)_{SCP,p} = \frac{2K_p}{c}\langle 1_p|Q_p|0_p\rangle^2[45aG'_p{}^2 + 13\beta^2_{Gp} - \beta^2_{Ap} + \cos(\theta)(90aG'_p{}^2 - 10\beta^2_{Gp} - 6\beta^2_{Ap}) + \cos^2(\theta)(45aG'_p{}^2 + \beta^2_{Gp} + 3\beta^2_{Ap})]\, d\Omega \quad (1)$$

To express σ in m^2 (SI units are used throughout this work), the constant K_p is given by

$$K_p = \frac{1}{90}\left(\frac{\mu_0}{4\pi}\right)^2 \omega_p{}^3\omega_0 \quad (2)$$

where $\omega_0 = 2\pi\nu_0$ is the angular frequency of the laser beam, ω_p is the angular frequency of the scattered light, and μ_0 is the permeability constant. In the harmonic approximation, for a fundamental vibrational transition $(1_p \leftarrow 0_p)$

$$\langle 1_p|Q_p|0_p\rangle^2 = \hbar/(2\Delta\omega_p) \quad (3)$$

where $\Delta\omega_p$ corresponds to the vibrational transition associated with the normal coordinate Q_p. In the specific case of a backward-scattering $(\theta = \pi)$ setup, which is considered in the following simulations, eq 1 then reads

$$-\Delta^{n}\, d\sigma(\pi)_{SCP,p} = \frac{1}{90}\left(\frac{\mu_0}{4\pi}\right)^2 \omega_p{}^3\omega_0\frac{\hbar}{2\Delta\omega_p}\frac{2}{c}(24\beta^2_{Gp} + 8\beta^2_{Ap})\, d\Omega \quad (4)$$

The three invariants in eq 1 (aG'_p, β^2_{Gp}, and β^2_{Ap}) require the evaluation of the first-order derivatives of three polarizability tensors: $(\partial\alpha/\partial Q_p)$, $(\partial A/\partial Q_p)$, and $(\partial G'/\partial Q_p)$. A review by Buckingham[41] defines all of these polarizabilities. The invariants then have the form

$$aG'_p = \frac{1}{9}\sum_{\mu,\nu}\left(\frac{\partial\alpha_{\mu\mu}}{\partial Q_p}\right)_0\left(\frac{\partial G'_{\nu\nu}}{\partial Q_p}\right)_0 \quad (5)$$

$$\beta^2_{Gp} = \frac{1}{2}\sum_{\mu,\nu}\left[3\left(\frac{\partial\alpha_{\mu\nu}}{\partial Q_p}\right)_0\left(\frac{\partial G'_{\mu\nu}}{\partial Q_p}\right)_0 - \left(\frac{\partial\alpha_{\mu\mu}}{\partial Q_p}\right)_0\left(\frac{\partial G'_{\nu\nu}}{\partial Q_p}\right)_0\right] \quad (6)$$

$$\beta^2_{Ap} = \frac{\omega_0}{2}\sum_{\mu,\nu}\sum_{\lambda,\kappa}\left[\left(\frac{\partial\alpha_{\mu\nu}}{\partial Q_p}\right)_0\left(\varepsilon_{\mu\lambda\kappa}\frac{\partial A_{\lambda\kappa\nu}}{\partial Q_p}\right)_0\right] \quad (7)$$

To analyze the VROA intensity of a normal mode, we use the decomposition scheme called the group coupling matrix (GCM) introduced by Hug[42]

$$J_p = \sum_{i,j}^{N}\sum_{\alpha,\beta}^{3} L^x_{i\alpha,p}V(J)_{i\alpha,j\beta}L^x_{j\beta,p} = \sum_{i,j} J_{ij,p} \quad (8)$$

where $\underline{\underline{L}}^x$ is the Cartesian displacement matrix of the normal modes normalized so that $\Sigma_{i,\alpha}m_i(L^x_{i\alpha,p})^2 = 1$ and with $V_{i\alpha,j\beta}$ for $J = aG'$, β^2_G, or β^2_A given by

$$V(aG')_{i\alpha,j\beta} = \frac{1}{9}\sum_{\mu,\nu}\left(\frac{\partial\alpha_{\mu\mu}}{\partial R_{i\alpha}}\right)_0\left(\frac{\partial G'_{\nu\nu}}{\partial R_{j\beta}}\right)_0 \quad (9)$$

$$V(\beta^2_G)_{i\alpha,j\beta} = \frac{1}{2}\sum_{\mu,\nu}\left[3\left(\frac{\partial\alpha_{\mu\nu}}{\partial R_{i\alpha}}\right)_0\left(\frac{\partial G'_{\mu}}{\partial R_{j\beta}}\right)_0 - \left(\frac{\partial\alpha_{\mu\mu}}{\partial R_{i\alpha}}\right)_0\left(\frac{\partial G'_{\nu\nu}}{\partial R_{j\beta}}\right)_0\right] \quad (10)$$

$$V(\beta^2_A)_{i\alpha,j\beta} = \frac{\omega_0}{2}\sum_{\mu,\nu}\sum_{\lambda,\kappa}\left[\left(\frac{\partial\alpha_{\mu\nu}}{\partial R_{i\alpha}}\right)_0\left(\varepsilon_{\mu\lambda\kappa}\frac{\partial A_{\lambda\kappa\nu}}{\partial R_{j\beta}}\right)_0\right] \quad (11)$$

In the above summations, the indices μ, ν, λ, and κ are components of the electric or magnetic fields (x, y, z). The subscript 0 indicates that the properties are evaluated at the equilibrium geometry. The indices i and j stand for atoms, whereas α and β are used for Cartesian components (x, y, z). $\varepsilon_{\mu\lambda\kappa}$ is the antisymmetric unit tensor of Levi-Civita.

Using the previous summation (eq 8), the VROA intensity for a given normal mode of vibration p can be decomposed into

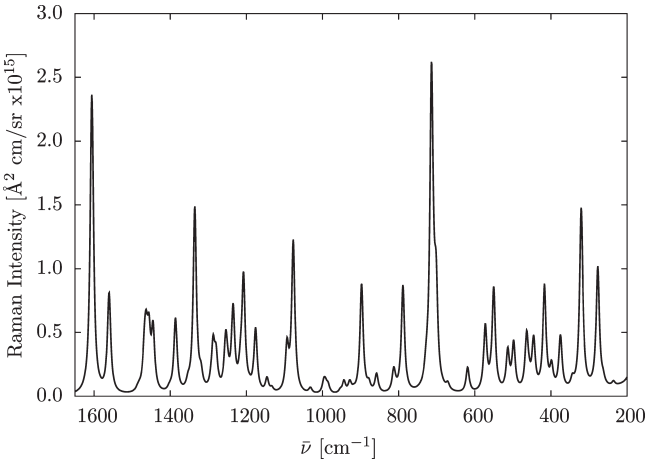

Figure 3. Simulated Raman polarized spectrum of (*S*,*S*)-Tröger's base. The vibrational normal coordinates were evaluated at the B3LYP/6-31G* level, whereas the polarizabilities and their geometrical derivatives were evaluated at the TDHF/rDPS:3-21G level. Each transition is represented by a Lorentzian function with a fwhm of 10 cm^{-1}. The optical wavelength was 532 nm, and a multiplicative factor of 0.96 was used to scale the vibrational frequencies.

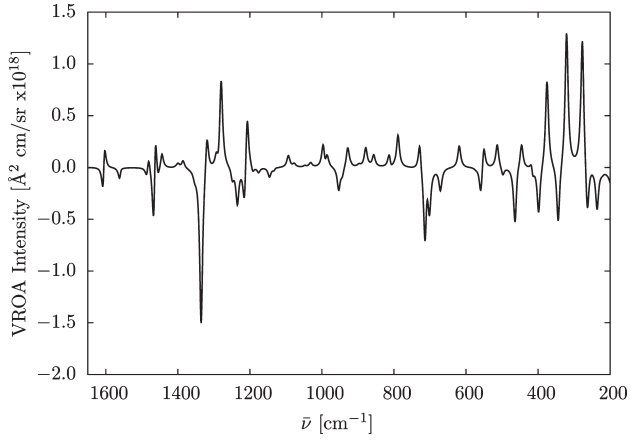

Figure 4. Simulated VROA backward-scattering spectrum of (*S*,*S*)-Tröger's base. The vibrational normal coordinates were evaluated at the B3LYP/6-31G* level, whereas the polarizabilities and their geometrical derivatives were evaluated at the TDHF/rDPS:3-21G level. Each transition is represented by a Lorentzian function with a fwhm of 10 cm^{-1}. The optical wavelength was 532 nm, and a multiplicative factor of 0.96 was used to scale the vibrational frequencies.

homonuclear ($J_{ii,p}$) and heteronuclear ($J_{ij,p}$) contributions. Then, using straightforward summations, these definitions can be generalized to groups of atoms. The diagonal terms are mononuclear or intragroup, whereas the off-diagonal terms are dinuclear or intergroup. As only the symmetric part contributes to the total intensity of the vibrational modes, they are best represented by upper triangular matrices, with off-diagonal elements equal to the sum of the two off-diagonal halves of the full matrix. In the GCM scheme of Hug,[42] the matrix elements are visualized as circles, with an area proportional to the $J_{ij,p}$ values, whereas their color is related to their sign. The factor of proportionality is tunable but fixed throughout this work for consistency of analysis.

The atomic contribution patterns (ACPs) represent the atomic contributions of each atom to the total VROA intensity of a given mode *p*. They are obtained by taking the self-contributions of the atom ($J_{ii,p}$) and then splitting the dinuclear terms ($J_{ij,p}$) between the corresponding atoms in such a way that the resulting quasi-atomic quantities best reflect the contributions that each atom makes to VROA scattering through the combined action of the gradients of electronic tensors at its site and the motion of its nucleus.[42] Spheres are then drawn on each atom with their surface area proportional to the value of the contribution and their color reflecting the sign: red for positive and yellow for negative. Again, the factor of proportionality is tunable but fixed throughout this work.

Table 1. Raman Polarized and VROA Backward-Scattering Intensities of (*S*,*S*)-Tröger's Base Associated with the Normal Modes in the 1140−1400 cm^{-1} Wavenumber Range[a,b]

normal mode	freq	Raman intensity (Å²/sr × 10^{14})	VROA intensity (Å²/sr × 10^{17})
56 (B)	1145.62	0.171	−0.142
57 (A)	1175.97	**0.774**	−0.078
58 (B)	1192.00	0.033	−0.095
59 (A)	1207.47	**1.391**	**0.923**
60 (B)	1215.21	0.230	**−0.673**
61 (A)	1234.79	**1.003**	**−0.551**
62 (B)	1248.82	0.123	−0.185
63 (A)	1253.88	**0.624**	0.017
64 (B)	1279.75	**0.404**	**1.373**
65 (A)	1287.43	**0.546**	−0.193
66 (B)	1292.77	0.041	0.166
67 (A)	1316.98	0.017	0.058
68 (B)	1319.27	0.163	**0.553**
69 (A)	1335.30	**2.285**	**−2.427**
70 (B)	1353.18	0.089	−0.096
71 (B)	1385.95	0.296	0.268
72 (A)	1386.31	**0.617**	−0.156

[a] Symmetry of the modes given in parentheses (C_2 point group). [b] Largest intensities highlighted in boldface.

3. COMPUTATIONAL METHODOLOGY

The structures as well as the vibrational frequencies and normal modes were determined using the analytical coupled-perturbed Kohn−Sham[43] procedure together with the 6-31G* basis set.[44] The hybrid B3LYP exchange-correlation functional was selected owing to its recognized performance for calculating vibrational frequencies.[45] However, to account for the systematic error due to missing electron correlation and anharmonicity effects, a multiplicative factor of 0.96[45,46] was employed to scale the B3LYP vibrational frequencies.

The geometry derivatives of the three polarizability tensors entering into the Raman and VROA invariants were calculated using a fully analytical procedure[47] within the time-dependent Hartree−Fock (TDHF) scheme. Because of the relatively large size of the system but also because of its recognized performance, the rDPS:3-21G (reduced diffuse polarization function and shell augmented) basis set introduced by Zuber and Hug[48] was employed. It consists of the 3-21++G[49] basis set augmented by a set of p diffuse functions (of exponent 0.2) on the hydrogen atoms. The derivatives were evaluated for the Cartesian displacements and then transformed into geometrical derivatives with respect to the vibrational normal coordinates, with the normal

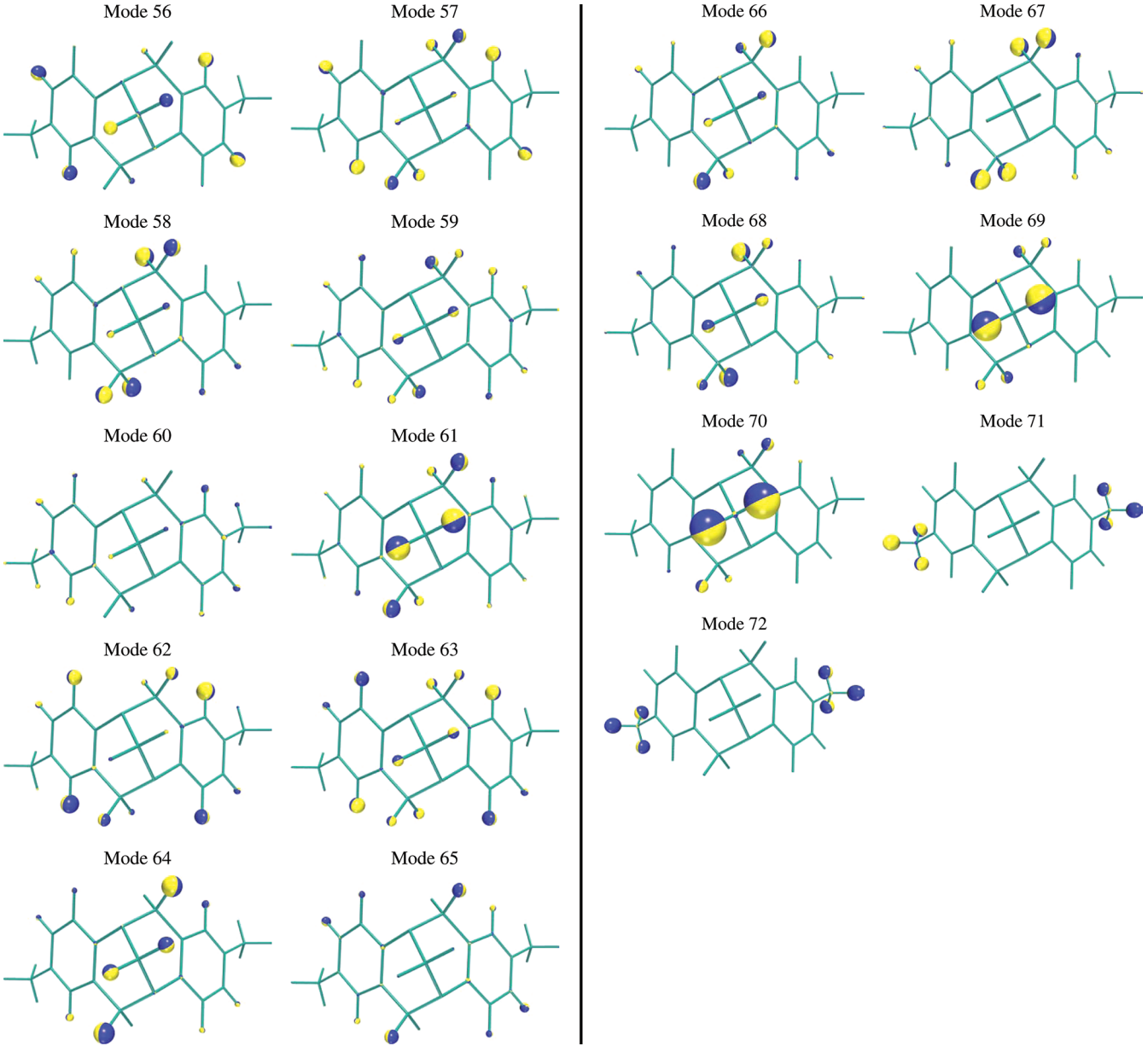

Figure 5. Sketch of the B3LYP/6-31G* vibrational normal modes of (*S*,*S*)-Tröger's base in the 1140−1400 cm^{-1} wavenumber range. The direction of atomic displacements is perpendicular to the junction plane between the two hemispheres of distinct color, and their amplitudes are proportional to the radius of the sphere.

coordinates calculated using the coupled-perturbed Kohn−Sham (CPKS) procedure.

The calculations were performed using both the DALTON[50] and Gaussian 03[51] quantum chemistry packages. The DALTON program was used to obtain the analytical geometry derivatives (at the time-dependent Hartree−Fock level of theory) of the dynamic tensors: $(\partial\alpha/\partial X)$, $(\partial A/\partial X)$, and $(\partial G'/\partial X)$. Gaussian 03 was used to optimize the geometries and to determine the vibrational normal modes and frequencies.

One should note that more avanced quantum mechanical methods such as coupled cluster for such calculations are still in their infancy,[52] whereas such methods have existed for optical rotation for quite some time now.[53−55]

A typical incident light wavelength of 532 nm was employed in all optical tensor calculations. This wavelength is clearly in the off-resonance regime. A Maxwell−Boltzmann *T*-dependence factor $(1/\{1 - \exp[-\hbar\Delta\omega_p/(k_bT)]\})$ was added to eq 4 with $T = 298.15$ K to account for the *T* dependence of the populations of the vibrational levels. In the spectra, each transition is represented by a Lorentzian function with a full width at half-maximum (fwhm) of 10 cm^{-1}, which is more or less what is observed in the experimental spectra.[56]

Pictures of molecular structures, the vibrational normal modes, the atomic contribution patterns (ACPs), and group coupling matrices (GCMs) were prepared with the PyVib2 program.[57,58]

4. SIMULATION AND INTERPRETATION OF SPECTRA

The B3LYP/6-31G*-optimized structure of (*S*,*S*)-Tröger's base is depicted in Figure 1. Figure 2 shows the infrared spectrum

Table 2. $\langle \tilde{Q}_s^{\mathrm{fragL}} | \tilde{Q}_p^{\mathrm{fragL}} \rangle$ Overlaps between the B3LYP/6-31G* Fragment Modes on One-Half of the Tröger's Base Molecule in the 1140−1400 cm^{-1} Wavenumber Range

	56	57	58	59	60	61	62	63	64	65	66	67	68	69	70	71	72
56	**0.454**	**−0.325**	−0.013	−0.081	−0.016	0.070	0.012	0.033	−0.015	−0.021	−0.010	−0.010	0.022	−0.003	0.025	0.001	0.000
57	**−0.325**	**0.499**	0.066	−0.001	0.056	0.001	−0.060	0.001	**0.136**	0.001	**0.242**	0.000	**−0.124**	−0.001	**−0.143**	−0.002	0.000
58	−0.013	0.066	**0.497**	0.018	−0.005	**−0.172**	0.003	−0.079	−0.004	**−0.177**	−0.003	0.000	0.006	**0.302**	0.006	0.000	−0.004
59	−0.081	−0.001	0.018	**0.499**	**0.417**	0.002	−0.017	0.001	−0.074	0.001	**−0.154**	0.000	−0.003	−0.002	−0.088	−0.001	0.000
60	−0.016	0.056	−0.005	**0.417**	**0.494**	**0.231**	0.004	0.075	−0.005	−0.022	−0.003	0.008	0.008	0.026	0.010	0.000	0.000
61	0.070	0.001	**−0.172**	0.002	**0.231**	**0.498**	**0.205**	−0.001	0.071	−0.001	**0.185**	0.000	0.067	0.003	**0.197**	0.005	0.000
62	0.012	−0.060	0.003	−0.017	0.004	**0.205**	**0.497**	**−0.437**	0.005	0.023	0.004	0.029	−0.006	0.013	−0.004	0.000	−0.001
63	0.033	0.001	−0.079	0.001	0.075	−0.001	**−0.437**	**0.499**	0.021	0.000	0.008	0.000	0.053	0.001	0.133	0.005	0.000
64	−0.015	**0.136**	−0.004	−0.074	−0.005	0.071	0.005	0.021	**0.483**	**0.364**	−0.016	**−0.111**	0.008	**0.222**	−0.016	0.000	0.001
65	−0.021	0.001	**−0.177**	0.001	−0.022	−0.001	0.023	0.000	**0.364**	**0.500**	**−0.263**	0.000	−0.054	0.001	−0.056	0.003	0.000
66	−0.010	**0.242**	−0.003	**−0.154**	−0.003	**0.185**	0.004	0.008	−0.016	**−0.263**	**0.484**	−0.092	0.005	−0.014	−0.021	0.000	−0.001
67	−0.010	0.000	0.000	0.000	0.008	0.000	0.029	0.000	−0.111	0.000	−0.092	**0.499**	**−0.431**	0.000	**0.174**	−0.004	0.000
68	0.022	**−0.124**	0.006	−0.003	0.008	0.067	−0.006	0.053	0.008	−0.054	0.005	**−0.431**	**0.491**	0.010	−0.011	0.000	0.005
69	−0.003	−0.001	**0.302**	−0.002	0.026	0.003	0.013	0.001	**0.222**	0.001	−0.014	0.000	0.010	**0.497**	**0.194**	−0.002	0.000
70	0.025	**−0.143**	0.006	−0.088	0.010	**0.197**	−0.004	**0.133**	−0.016	−0.056	−0.021	0.174	−0.011	**0.194**	**0.437**	0.000	0.000
71	0.001	−0.002	0.000	−0.001	0.000	0.005	0.000	0.005	0.000	0.003	0.000	−0.004	0.000	−0.002	0.000	**0.510**	**−0.499**
72	0.000	0.000	−0.004	0.000	0.000	0.000	−0.001	0.000	0.001	0.000	−0.001	0.000	0.005	0.000	0.000	**−0.499**	**0.490**

calculated at the B3LYP/6-31G* level of theory. This spectrum is similar to the calculated spectrum and therefore in close agreement with the experimental one published by Aamouche and coworkers.[15] The spectrum simulated using the Cartesian derivatives of the dipole moment at the TDHF/rDPS:3-21G level of theory is also reproduced in Figure 2. Only small differences in the relative intensities are observed between the B3LYP/6-31G* and the TDHF/rDPS:3-21G intensities (for instance, the peak at 812 cm^{-1} is more intense for the latter), which again shows the good performance of this small basis set.[48]

The Raman polarized (Figure 3) and VROA backward-scattering (Figure 4) spectra were then simulated. The Raman spectrum is dominated by a succession of peaks, whereas the VROA spectrum displays clearer signatures such as the intense positive−negative doublet around 1300 cm^{-1}. The Raman and VROA intensities for the modes within the 1140−1400 cm^{-1} range are listed in Table 1. One observes that, in this range, nearly all of the modes associated with the irreducible representation A (C_2 point group) are Raman-intense, whereas the modes associated with the irreducible representation B have smaller Raman intensities (except for mode 64). Such behavior is not observed for the VROA intensities, where fewer modes with large intensities are found. Indeed, the VROA spectrum in this range is dominated by three positive−negative−positive peaks around 1215 cm^{-1} (modes 59−61) and by the positive−negative couplet around 1300 cm^{-1} (modes 64 and 69). The vibrational normal modes sketched in Figure 5 mainly involve wagging and twisting motions of the hydrogen atoms.

To better understand the relationship between the vibrational normal modes, one can split any normal mode of Tröger's base into two fragments (L and R for left and right, respectively) following the C_2 symmetry of the molecule

$$\begin{aligned} |Q_p\rangle &= \sum_{i}^{N} \sum_{\alpha}^{3} |X_{i\alpha}\rangle\langle X_{i\alpha}|Q_p\rangle \\ &= \sum_{i}^{\mathrm{fragL}} \sum_{\alpha}^{3} |X_{i\alpha}\rangle\langle X_{i\alpha}|Q_p\rangle + \sum_{i}^{\mathrm{fragR}} \sum_{\alpha}^{3} |X_{i\alpha}\rangle\langle X_{i\alpha}|Q_p\rangle \end{aligned} \tag{12}$$

or

$$|Q_p\rangle = |\tilde{Q}_p^{\mathrm{fragL}}\rangle + |\tilde{Q}_p^{\mathrm{fragR}}\rangle \tag{13}$$

where $\langle X_{i\alpha}|Q_p\rangle = L_{i\alpha,p}$ is the element of the unitary matrix that diagonalizes the mass-weighted Hessian associated with atom i in the Cartesian direction α for eigenvector p. One can then define the fragment modes $|\tilde{Q}_p^{\mathrm{fragL}}\rangle$ and $|\tilde{Q}_p^{\mathrm{fragR}}\rangle$. The overlap between two normal modes, s and p, can therefore be rewritten as

$$\begin{aligned} \langle Q_s|Q_p\rangle &= \delta_{sp} \\ &= \langle \tilde{Q}_s^{\mathrm{fragL}}|\tilde{Q}_p^{\mathrm{fragL}}\rangle + \langle \tilde{Q}_s^{\mathrm{fragR}}|\tilde{Q}_p^{\mathrm{fragR}}\rangle \end{aligned} \tag{14}$$

The overlaps between these fragment modes can help in analyzing the relationship between the normal modes. Indeed, for a model system where the modes come in pairs with irreducible representations A and B, the overlap $\langle \tilde{Q}_s^{\mathrm{fragL}}|\tilde{Q}_p^{\mathrm{fragL}}\rangle$ (and similarly $\langle \tilde{Q}_s^{\mathrm{fragR}}|\tilde{Q}_p^{\mathrm{fragR}}\rangle$) will consist of a block-diagonal matrix with all blocks having the following values

$$\langle \tilde{Q}^{\mathrm{fragL}}|\tilde{Q}^{\mathrm{fragL}}\rangle = \begin{pmatrix} 0.500 & -0.500 \\ -0.500 & 0.500 \end{pmatrix} \tag{15}$$

The sign of the two off-diagonal elements is arbitrary. The $\langle \tilde{Q}_s^{\mathrm{fragR}}|\tilde{Q}_p^{\mathrm{fragR}}\rangle$ matrix is the same but with opposite signs for both off-diagonal elements.

In the present case, fragment L consists of atoms N_1, C_4, C_6, C_7, C_8, C_9, C_{10}, C_{11}, C_{18}, and the corresponding hydrogen atoms plus one of the hydrogen atoms of C_3, whereas fragment R consists of atoms N_2, C_5, C_{12}, C_{13}, C_{14}, C_{15}, C_{16}, C_{17}, C_{19}, and the corresponding hydrogen atoms plus the other hydrogen atom attached to C_3. Note that in addition to fragments L and R, one needs to add the contribution of C_3 to eq 14 for the equation to be fulfilled as this carbon atom is on the C_2 axis of symmetry. Table 2 displays one of the two overlaps of eq 14 because the other one has the same diagonal elements and the opposite off-diagonal terms with a non-negligible amplitude. This matrix is not block-diagonal because all modes except modes 56, 71, and

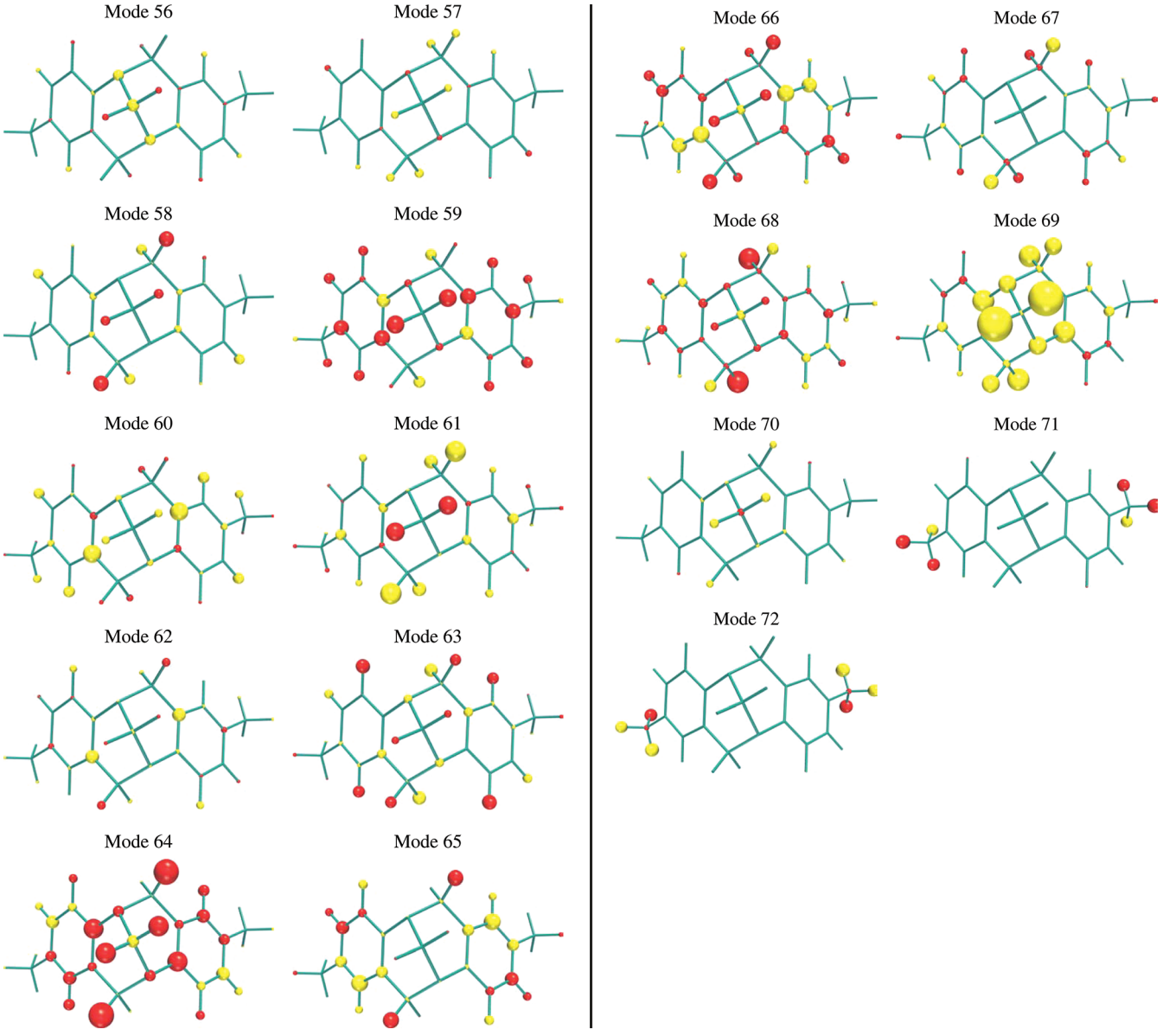

Figure 6. Sketch of the VROA backward-scattering atomic contribution patterns (ACPs) of (*S*,*S*)-Tröger's base associated with vibrational normal modes in the 1140−1400 cm^{-1} wavenumber range. The sphere surfaces of the ACPs are proportional to the VROA backward-scattering intensities. Positive intensities are represented by red spheres, and negative ones are represented by yellow spheres.

72 have more than one off-diagonal terms that are important. Therefore all of the modes in this range have some similarities except for modes 71 and 72, which form a perfect pair of modes. This behavior can also been seen in the sketch of the normal modes (Figure 5).

The atomic contribution patterns to the VROA backward-scattering intensities are given in Figure 6, and the group coupling matrices for the six most intense VROA peaks in the region under study are depicted in Figure 7. In all of these data, one can observe that the intensity arises mostly from the hydrogen atoms, especially those that are close to the two chiral centers, namely H_3, H_4, and H_5. The carbon atoms C_{11} and C_{13} close to the nitrogen atoms also contribute significantly to the VROA intensity (see the ACP for modes 64 and 69). The terms that contribute the most to the group coupling matrices are the couplings between groups B−B, C−C, and B−C where group A contains the two nitrogen atoms, group B contains the neighboring carbon atoms (C_3, C_4, C_5, C_{11}, C_{13}), group C contains the hydrogen atoms bonded to these neighboring carbon atoms ($2H_3$, $2H_4$, $2H_5$) and group D contains the rest of the atoms. Minimal contributions are actually coming from the chiral nitrogen atoms themselves.

5. CONCLUSIONS

The Raman and VROA spectra of (*S*,*S*)-Tröger's base have been simulated using a combined DFT/TDHF approach. We mainly discussed the peaks in the 1140−1400 cm^{-1} wavenumber range because the VROA signatures in this range are intense. In this region, nearly all of the Raman-active bands belong to the irreducible representation A (C_2 point group), but this is not the case for the VROA spectrum. The vibrational normal modes associated with the peaks in this range mainly consist of wagging

dx.doi.org/10.1021/jp208591j |*J. Phys. Chem. A* 2011, 115, 13706–13713

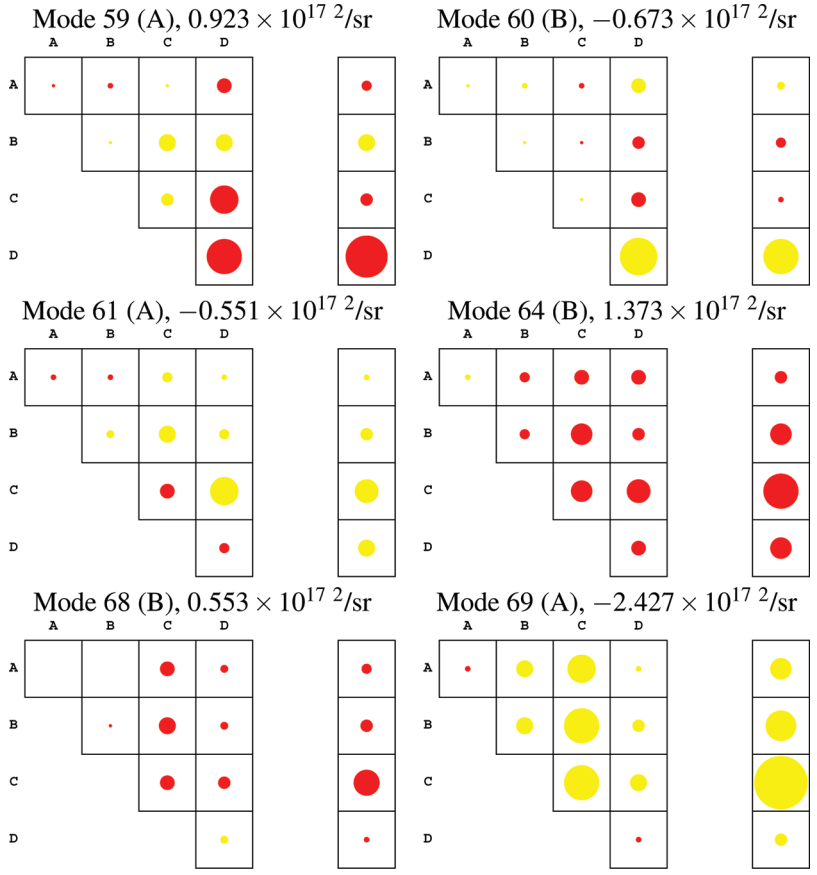

Figure 7. Sketch of the VROA backward-scattering group coupling matrices (GCMs) of (*S*,*S*)-Tröger's base associated with vibrational normal modes in the 1140−1400 cm^{-1} wavenumber range. The groups are as follows: A = [N_1, N_2], B = [C_3, C_4, C_5, C_{11}, C_{13}], C = [$2H_3$, $2H_4$, $2H_5$], and D = [other atoms] (see Figure 1 for the numbering of the atoms). The areas of the circles are directly proportional to the coupling contributions, with red (yellow) indicating positive (negative) contributions.

and twisting motions of the hydrogen atoms. From the atomic contribution patterns (ACPs) and group coupling matrices (GCMs), one finds that the VROA backward-scattering intensities mainly arise from hydrogen and carbon atoms in the vicinity of the two chiral nitrogen atoms. The VROA signatures in the 1140−1400 cm^{-1} range are therefore a fingerprint of the local chirality around the two chiral nitrogen centers.

AUTHOR INFORMATION

Corresponding Author

*E-mail: vincent.liegeois@fundp.ac.be.

ACKNOWLEDGMENT

V.L. thanks the F.R.S.-FNRS for his Postdoctoral Researcher position. The calculations were performed on the Interuniversity Scientific Computing Facility (ISCF), installed at the Facultés Universitaires Notre-Dame de la Paix (Namur, Belgium), for which the authors gratefully acknowledge the financial support of the F.R.S.-FRFC (Grant 2.4.617.07.F) and of the FUNDP.

REFERENCES

(1) Tröger, J. *J. Prakt. Chem.* **1887**, *36*, 225–245.
(2) Prelog, V.; Wieland, P. *Helv. Chim. Acta* **1944**, *27*, 1127–1134.
(3) Lemaur, V.; Cornil, J.; Didier, D.; Mujawase, A.; Sergeyev, S. *Helv. Chim. Acta* **2007**, *90*, 2087–2095.
(4) Xin, Q.; Tao, X.-T.; Wang, F.-Z.; Sun, J.-L.; Zou, D.-C.; Wang, F.-J.; Liu, H.-J.; Liu, Z.; Ren, Y.; Jiang, M.-H. *Org. Electron.* **2008**, *9*, 1076–1086.
(5) Yuan, C.-X.; Tao, X.-T.; Wang, L.; Yang, J.-X.; Jiang, M.-H. *J. Phys. Chem. C* **2009**, *113*, 6809–6814.
(6) Schanne-Klein, M.; Boulesteix, T.; Hache, F.; Alexandre, M.; Lemercier, G.; Andraud, C. *Chem. Phys. Lett.* **2002**, *362*, 103–108.
(7) Sergeyev, S.; Didier, D.; Boitsov, V.; Teshome, A.; Asselberghs, I.; Clays, K.; Velde, C. M. L. V.; Plaquet, A.; Champagne, B. *Chem.—Eur. J.* **2010**, *16*, 8181–8190.
(8) Satishkumar, S.; Periasamy, M. *Tetrahedron: Asymmetry* **2009**, *20*, 2257–2262.
(9) Sergeyev, S. *Helv. Chim. Acta* **2009**, *92*, 415–444.
(10) Mason, S. F.; Vane, G. W.; Schofield, K.; Wells, R. J.; Whitehurst, J. S. *J. Chem. Soc. B* **1967**, 553–556.
(11) Larson, S. B.; Wilcox, C. *Acta Crystallogr. C* **1986**, *42*, 224–227.
(12) Wilcox, C. *Tetrahedron Lett.* **1985**, *26*, 5749–5752.
(13) Wilem, S. H.; Qi, J. Z.; Williard, P. G. *J. Org. Chem.* **1991**, *56*, 485–487.
(14) Aamouche, A.; Devlin, F. J.; Stephens, P. J. *Chem. Commun.* **1999**, 361–362.
(15) Aamouche, A.; Devlin, F. J.; Stephens, P. J. *J. Am. Chem. Soc.* **2000**, *122*, 2346–2354.
(16) Barron, L. D.; Buckingham, A. D. *Mol. Phys.* **1971**, *20*, 1111–1119.
(17) Hug, W. In *Handbook of Vibrational Spectroscopy*; Chalmers, J. M., Griffiths, P. R., Eds.; John Wiley and Sons, 2002; p 175.

(18) Barron, L. D. *Molecular Light Scattering and Optical Activity*, 2nd ed.; Cambridge University Press: New York, 2004.
(19) Kaminsky, J.; Kapitan, J.; Baumruk, V.; Bednarova, L.; Bour, P. *J. Phys. Chem. A* **2009**, *113*, 3594–3601.
(20) Hudecova, J.; Kapitan, J.; Baumruk, V.; Hammer, R. P.; Keiderling, T. A.; Bour, P. *J. Phys. Chem. A* **2010**, *114*, 7642–7651.
(21) Yaffe, N. R.; Almond, A.; Blanch, E. W. *J. Am. Chem. Soc.* **2010**, *132*, 10654–10655.
(22) Kinalwa, M. N.; Blanch, E. W.; Doig, A. J. *Anal. Chem.* **2010**, *82*, 6347–6349.
(23) Yamamoto, S.; Straka, M.; Watarai, H.; Bour, P. *Phys. Chem. Chem. Phys.* **2010**, *12*, 11021–11032.
(24) Pecul, M.; Deillon, C.; Thorvaldsen, A. J.; Ruud, K. *J. Raman Spectrosc.* **2010**, *41*, 1200–1210.
(25) Nieto-Ortega, B.; Casado, J.; Blanch, E. W.; Lopez Navarrete, J. T.; Quesada, A. R.; Ramirez, F. J. *J. Phys. Chem. A* **2011**, *115*, 2752–2755.
(26) Cheeseman, J. R.; Shaik, M. S.; Popelier, P. L. A.; Blanch, E. W. *J. Am. Chem. Soc.* **2011**, *133*, 4991–4997.
(27) Johannessen, C.; Pendrill, R.; Widmalm, G.; Hecht, L.; Barron, L. D. *Angew. Chem., Int. Ed.* **2011**, *50*, 5349–5351.
(28) Qiu, S.; Li, G.; Wang, P.; Zhou, J.; Feng, Z.; Li, C. *J. Phys. Chem. A* **2011**, *114*, 1340−1349.
(29) Weymuth, T.; Jacob, C. R.; Reiher, M. *ChemPhysChem* **2011**, *12*, 1165–1175.
(30) Yamamoto, S.; Watarai, H.; Bour, P. *ChemPhysChem* **2011**, *12*, 1509–1518.
(31) Hopmann, K. H.; Ruud, K.; Pecul, M.; Kudelski, A.; Dra)nský, M.; Bour, P. *J. Phys. Chem. B* **2011**, *115*, 4128–4137.
(32) Luber, S.; Reiher, M. *Chem. Phys.* **2008**, *346*, 212–223.
(33) Luber, S.; Reiher, M. *ChemPhysChem* **2010**, *11*, 1876–1887.
(34) Johannessen, C.; Hecht, L.; Merten, C. *ChemPhysChem* **2011**, *12*, 1419–1421.
(35) Reiher, M.; Liégeois, V.; Ruud, K. *J. Phys. Chem. A* **2005**, *109*, 7567–7574.
(36) Liégeois, V. *ChemPhysChem* **2009**, *10*, 2017–2025.
(37) Kapitan, J.; Johannessen, C.; Bour, P.; Hecht, L.; Barron, L. D. *Chirality* **2010**, *21*, E4–E12.
(38) Lamparska, E.; Liégeois, V.; Quinet, O.; Champagne, B. *ChemPhysChem* **2006**, *7*, 2366–2376.
(39) Liégeois, V.; Jacob, C. R.; Champagne, B.; Reiher, M. *J. Phys. Chem. A* **2010**, *114*, 7198–7212.
(40) Drooghaag, X.; Marchand-Brynaert, J.; Champagne, B.; Liégeois, V. *J. Phys. Chem. B* **2010**, *114*, 11753–11760.
(41) Buckingham, A. D. *Adv. Chem. Phys.* **1967**, *12*, 107.
(42) Hug, W. *Chem. Phys.* **2001**, *264*, 53–69.
(43) Komornicki, A.; Fitzgerald, G. *J. Chem. Phys.* **1993**, *98*, 1398–1421.
(44) Hehre, W. J.; Ditchfield, R.; Pople, J. A. *J. Chem. Phys.* **1972**, *56*, 2257.
(45) Scott, A. P.; Radom, L. *J. Phys. Chem.* **1996**, *100*, 16502–16513.
(46) Irikura, K. K.; Johnson, R. D., III; Kacker, R. N. *J. Phys. Chem. A* **2005**, *109*, 8430–8437.
(47) Liégeois, V.; Ruud, K.; Champagne, B. *J. Chem. Phys.* **2007**, *127*, 204105.
(48) Zuber, G.; Hug, W. *J. Phys. Chem. A* **2004**, *108*, 2108–2118.
(49) Binkley, J. S.; Pople, J. A.; Hehre, W. J. *J. Am. Chem. Soc.* **1980**, *102*, 939.
(50) *DALTON, A Molecular Electronic Structure Program*, release 2.0, 2005; see http://dirac.chem.sdu.dk/daltonprogram.org/. Accessed January 2011.
(51) Frisch, M. J.; Trucks, G. W.; Schlegel, H. B.; Scuseria, G. E.; Robb, M. A.; Cheeseman, J. R.; Scalmani, G.; Barone, V.; Mennucci, B.; Petersson, G. A.; Nakatsuji, H.; Caricato, M.; Li, X.; Hratchian, H. P.; Izmaylov, A. F.; Bloino, J.; Zheng, G.; Sonnenberg, J. L.; Hada, M.; Ehara, M.; Toyota, K.; Fukuda, R.; Hasegawa, J.; Ishida, M.; Nakajima, T.; Honda, Y.; Kitao, O.; Nakai, H.; Vreven, T.; Montgomery, J. A., Jr.; Peralta, J. E.; Ogliaro, F.; Bearpark, M.; Heyd, J. J.; Brothers, E.; Kudin, K. N.; Staroverov, V. N.; Kobayashi, R.; Normand, J.; Raghavachari, K.; Rendell, A.; Burant, J. C.; Iyengar, S. S.; Tomasi, J.; Cossi, M.; Rega, N. ; Millam, J. M.; Klene, M.; Knox, J. E.; Cross, J. B.; Bakken, V.; Adamo, C; Jaramillo, J.; Gomperts, R. E.; Stratmann, O.; Yazyev, A. J.; Austin, R.; Cammi, C.; Pomelli, J. W.; Ochterski, R.; Martin, R. L.; Morokuma, K.; Zakrzewski, V. G.; Voth, G. A.; Salvador, P.; Dannenberg, J. J.; Dapprich, S.; Daniels, A. D.; Farkas, O.; Foresman, J. B.; Ortiz, J. V.; Cioslowski, J.; Fox, D. J. *Gaussian* 03, revision B.04; Gaussian Inc.: Wallingford, CT, 2009.
(52) Crawford, T. D.; Ruud, K. *ChemPhysChem*, published online Sep 14, 2011, http://dx.doi.org/10.1002/cphc.201100547.
(53) Mach, T. J.; Crawford, T. D. *J. Phys. Chem. A* **2011**, *115*, 10045.
(54) Pedersen, T. B.; Kongsted, J.; Crawford, T. D. *Chirality* **2009**, *21*, E68–E75.
(55) Tam, M. C.; Russ, N. J.; Crawford, T. D. *J. Chem. Phys.* **2004**, *121*, 3550–3557.
(56) Zuber, G.; Hug, W. *Helv. Chim. Acta* **2004**, *87*, 2208–2234.
(57) Fedorovsky, M. *PyVib2, A Program for Analyzing Vibrational Motion and Vibrational Spectra*, 2007; see http://pyvib2.sourceforge.net. Accessed January 2011.
(58) Fedorovsky, M. *Comput. Lett.* **2006**, *2*, 233–236.